Applied Catalysis A, General 661 (2023) 119233

Contents lists available at ScienceDirect

Applied Catalysis A, General

journal homepage: www.elsevier.com/locate/apcata

Photoelectrochemical hydrogen evolution on macroscopic electrodes of exfoliated SnSe flakes

Qianqian Ba [a], Péter S. Tóth [a,*], Ádám Vass [a], Krishnan Rajeshwar [b,*], Csaba Janáky [a]

[a] Department of Physical Chemistry and Materials Science, Interdisciplinary Excellence Center, University of Szeged, Rerrich Sq. 1, Szeged H6720, Hungary
[b] Department of Chemistry and Biochemistry, The University of Texas at Arlington, TX, USA

ARTICLE INFO

Keywords:
Liquid phase exfoliation
Layered semiconductor
Photoelectrochemical kinetics
Size-control
Pt catalyst

ABSTRACT

Tin(II) selenide (SnSe) is an attractive photocathode candidate for performing photoelectrochemical (PEC) hydrogen evolution reaction (HER), because of its negative conduction band position relative to the HER redox level and a high absorption coefficient for efficiently harvesting solar energy. To prepare thinner layered SnSe flakes from larger size commercial SnSe crystals, liquid phase exfoliation (LPEx) was employed in isopropanol/water mixtures (IPA/H_2O) and pure IPA. Macroscopic (1 cm^2) electrodes were prepared from the exfoliated SnSe flakes by immobilizing them on glassy carbon electrodes. These flakes obtained by exfoliating the as-received commercial SnSe in pure IPA exhibited 10 times higher PEC activity than those prepared in IPA/H_2O. An additional size separation to make three different size fractions of SnSe crystals served to further optimize the LPEx process. Electrodes prepared from the largest flakes showed the highest photocurrent density of 2.44 ± 0.65 mA cm^{-2} at −0.74 V versus RHE under 1 Sun, and ~ 30% incident-photon-to-electron conversion efficiency at 900 nm. Decoration of the SnSe surface with Pt catalyst islands further improved the PEC activity to 4.39 ± 0.15 mA cm^{-2}. This photocurrent density represents the highest value reported to date on macroscopic electrodes assembled from SnSe.

1. Introduction

Photoelectrochemical hydrogen evolution reaction (PEC HER) is a promising method for the conversion of solar energy to chemical energy (i.e., hydrogen) [1,2]. A low-cost and properly functioning semiconductor photoelectrode constitutes the heart of such processes [3]. In recent decades, many semiconductors have been studied to fulfill this need [4–11], for example, metal oxides [4,5], metal chalcogenides [6–8], group IV, and group III-V compounds [9–11]. Among these materials, metal chalcogenides have attracted increasing attention because of their favorable electrical and optical properties [6–8,12–14]. Unfortunately, high PEC performance was achieved only on single crystal metal dichalcogenides or in microelectrochemical cells, implying a limitation in the scalability of this solar energy conversion approach [15,16]. There is a clear need to study macroelectrodes prepared from polycrystalline semiconductors, for example in the form of flakes, and identify the opportunities and barriers for their applications [14].

Tin(II) selenide (SnSe) is a binary group IV-VI monochalcogenide with a layered orthorhombic structure [17–20]. Because of its ultralow lattice thermal conductivity, it has been already extensively investigated in the field of thermoelectrics [21–23]. It has a high absorption coefficient of 10^5 cm^{-1}, and is a p-type semiconductor nature with a narrow energy bandgap (0.9–1.8 eV, corresponding to the thickness dependency from bulk to monolayer), making it a suitable candidate for photovoltaic and optoelectronic devices [24–26]. In addition, as a layered semiconductor, bulk SnSe can be exfoliated to thinner flakes because of the weak van der Waals force between the layers. Exfoliation in turn causes a change in the bandgap, which can be exploited in different PEC processes [18,27]. Furthermore, both Sn and Se elements have large abundance, and SnSe has low-toxicity, which makes this material even more attractive.

So far, various synthesis procedures have been reported for SnSe samples, such as hydrothermal method [28], chemical vapor deposition [26,29], electrodeposition [30–32], Li-intercalation exfoliation [33,34], and liquid phase exfoliation [27,35]. Most of these techniques, however, have their own drawbacks. For example, chemical vapor deposition generally requires a high reaction temperature and vacuum chamber [26]. Li-intercalation-based exfoliation may damage the crystallinity of the obtained flakes [18]. The hydrothermal method is not suitable for scaling-up a particular synthesis. Therefore, a facile and effective

* Corresponding authors.
E-mail addresses: toth.peter.sandor@chem.u-szeged.hu (P.S. Tóth), rajeshwar@uta.edu (K. Rajeshwar).

https://doi.org/10.1016/j.apcata.2023.119233
Received 27 September 2022; Received in revised form 3 April 2023; Accepted 23 April 2023
Available online 24 April 2023

approach is needed for the mass production of SnSe flakes to prepare electrodes with large geometric surface area. Liquid phase exfoliation (LPEx) is one such low-cost method affording high product yield, while employing a simple experimental setup. Hence, this method was deployed in this study.

This process has been widely used to obtain thin flakes from two-dimensional (2D) materials, such as graphene and transition metal dichalcogenides (TMDCs) [36,37]. Applying centrifugation at different speeds after the LPEx process is a simple way to separate the flakes based on their different size parameters, i.e., area and thickness [38]. The LPEx method was used to prepare high-quality crystalline SnSe nanosheets in isopropanol (IPA), and a tunable optical bandgap was found [27,35]. A sonication-assisted LPEx method was applied to produce few-layer SnSe nanosheets in different solvents (such as N-methyl-2-pyrrolidone, dimethylformamide, ethanol, IPA) and a thickness-dependent bandgap was confirmed [35].

Decoration of the semiconductor nanoflakes with catalyst islands is a viable approach to enhance PEC performance. Thus, Pt catalyst was deposited on the surface of different semiconductors to capture/store photogenerated electrons from the semiconductor conduction band and thereby minimize charge carrier recombination. This chemical modification strategy also opens up a reductive reaction pathway for the electrons, leading to better HER performance [39,40]. Photodeposition is a simple and common approach to prepare Pt-decorated semiconductor photocatalysts [41,42]. Table 1 summarizes the PEC HER performance of metal-chalcogenide macroelectrodes composed of flakes compared to our best-performing bare SnSe photocathode. In previous reports on TMDC flakes, the PEC HER performance has been limited to the μA cm^{-2} range reaching a maximum 1 mA cm^{-2} photocurrent density (using 150 mW cm^{-2} illumination) [7,35,43,44]. In the case of thermal vacuum evaporation prepared SnSe electrodes, somewhat higher 1.4 mA cm^{-2} photocurrent density was obtained under 1 Sun illumination.

In the spirit of exploring the full potential of the LPEx synthetic approach, we report here the preparation of SnSe photoelectrodes starting from commercial SnSe. The LPEx method was applied in different IPA/H_2O mixtures and pure IPA to prepare dispersions of SnSe flakes. A sieve process was then employed to separate the as-received commercial SnSe crystals to three size fractions prior to the LPEx process being subsequently carried out in pure IPA. This further improved the PEC performance of SnSe electrodes, reaching a level twice higher than using as-received SnSe. Finally, Pt nanoparticles were anchored on the surface of SnSe flakes using photodeposition, and the effect of different deposition parameters on the PEC performance was investigated. Under optimal conditions, Pt decorated SnSe gave twice higher PEC activity than bare SnSe. Using intensity modulated photocurrent spectroscopy (IMPS) we show below that, the Pt catalyst enhances the charge transfer process and suppresses charge carrier recombination at the electrode/electrolyte interface.

Table 1
Comparison of the PEC HER performance, measurement conditions, and preparation methods of transition metal chalcogenides-based photoelectrodes.

Material	j_{max} (mA cm^{-2})	Potential (V vs. RHE)	Conditions	Preparation method	Ref.
WSe_2	0.03	0	1 M H_2SO_4; 100 mW cm^{-2} (Cree MCE4 LED)	LPE	[7]
WSe_2	0.04	0	1 M H_2SO_4; 100 mW cm^{-2} (Xenon lamp)	LPE	[43]
WSe_2	~ 0.01	0.05	0.5 M H_2SO_4; 100 mW cm^{-2} (Xenon lamp)	aSLcS	[44]
MoS_2	~ 0.5	–0.5	0.5 M H_2SO_4; 150 mW cm^{-2} (Xenon lamp)	hydrothermal method	[45]
WS_2	~ 1	–0.5	0.5 M H_2SO_4; 150 mW cm^{-2} (Xenon lamp)	hydrothermal method	[45]
SnSe	1.4	–0.2	0.05 M H_2SO_4; 100 mW cm^{-2} (Optical fiber source, FX300)	thermal vacuum evaporation	[20]
SnSe	0.06	–1.0	1.5 M Na_2SO_3; 90 mW cm^{-2} (polychromatic lamp)	EC deposition	[32]
SnSe	0.02	–0.6	0.2 M $Eu(NO_3)_3$; 100 mW cm^{-2} (Xenon lamp)	EC deposition	[31]
SnSe	2.44	–0.74	0.5 M H_2SO_4; 100 mW cm^{-2} (Xenon lamp)	LPE	This work

2. Experimental

2.1. Materials

Tin selenide crystal (SnSe, 99.999%, diameter ≤ 12 mm, Alfa Aesar), isopropanol (IPA, 99.5%, Sigma-Aldrich), and sulphuric acid (H_2SO_4, 95%, VWR) were used without further purification. Ultrapure deionized water (Millipore Direct Q3-UV, 18.2 MΩ cm^{-1}) was employed in all the cases in the measurements described below. Glassy carbon plate (VWR, thickness: 2 mm, Type 2) was used as a substrate for electrode preparation.

2.2. Preparation of SnSe photoelectrocatalyst

SnSe flakes were produced by the LPEx of commercial layered SnSe crystals (as-received, named hereafter ar-SnSe) in IPA/H_2O mixtures with different IPA contents or in pure IPA. Fig. 1 shows the scheme for how the photoelectrocatalysts (i.e., flakes) were prepared.

First, the SnSe crystals were dispersed in the solvent with an initial concentration of 5 mg mL^{-1}, using a round-bottom flask, purging with Ar, and then sealed with parafilm. Then, the dispersion was processed by ultrasonication in a bath sonicator (Elmasonic P70H) operating at 37 kHz and 100% power for 12 h, while the temperature of the bath was kept below 30 °C with a recirculating cooler system (J. P. Selecta, Digiterm TFT). The unexfoliated and thicker pieces of the crystals were removed from the dispersion after ultrasonication followed by decantation. The obtained dispersion was then centrifuged at 100 g (Hermle centrifuge, Z366K) for 15 min at 15 °C. The supernatant was removed with a pipette (~90% of the total volume) leaving behind the sediment, which was collected from the bottom of the centrifuge tube. To determine the SnSe concentration in this sediment suspension, a certain volume was taken out to a vial, and then the mass of the vial was measured before and after a 1 h 110 °C drying process (hotplate, CAT Scientific, MCS78). This step was applied for every freshly prepared suspension. The SnSe flakes prepared from the ar-SnSe crystals in IPA/H_2O mixtures or pure IPA are denoted as IPA/H_2O-SnSe, and IPA-SnSe, respectively.

Size separation of the ar-SnSe crystals was performed in certain cases before the LPEx process, using a sieving system (Blau-Metall, Inc., with 200 mm in diameter sieves of woven wire mesh). This step resulted in three different fractions of SnSe crystals with 12–1.6 mm, 1.6–0.69 mm and 0.4–0.16 mm size ranges named as L-, M- and S-SnSe, respectively. The SnSe flakes prepared by the above mentioned LPEx process, in IPA from the size fractionated crystals, are named hereafter as L-IPA-, M-IPA- and S-IPA-SnSe, respectively.

2.3. Preparation of SnSe photoelectrodes

The as-prepared SnSe flakes were deposited on glassy carbon (GC) substrates ($A_{geometric}$ = 1 cm^2) by either using a modified Langmuir-

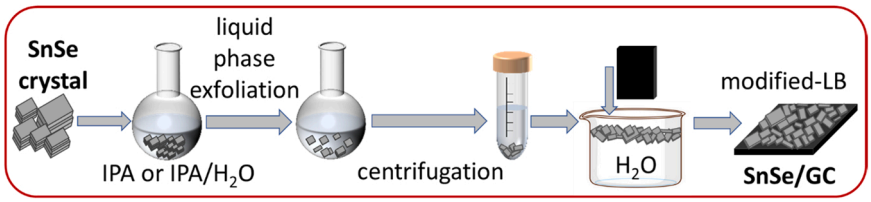

Fig. 1. Schematic illustration of liquid phase exfoliation of as-received SnSe crystals, selection of flakes using centrifugation, and preparation of SnSe flakes-based electrodes.

Blodgett (m-LB) method [14] (Fig. 1), or via spray-coating (Fig. 2). For the m-LB method, a beaker was filled with ultrapure deionized water, and the SnSe sediment suspension (from the centrifugation) was slowly dropped onto the surface of the water until film formation. Then, the GC substrate was inserted into the beaker and slowly removed by a tweezer, resulting in a film on the surface of the GC electrode. For spray coating, the concentration of the SnSe sediment-based suspension was set to 2 mg mL^{-1} by adjusting it with the same solvent used for LPEx process. Subsequently, the diluted suspension was spray-coated onto a GC pre-heated at 110 °C on a hot plate (Fig. 2). The mass loading of the SnSe films was measured in all cases.

2.4. Pt photodeposition on SnSe photoelectrodes

The Pt catalyst was photodeposited on the SnSe electrode surface from an aqueous electrolyte containing 5 mM H_2PtCl_6, 5 vol% methanol, and 0.25 mM H_2SO_4. Before deposition, the electrolyte was purged with Ar for 1 h in all cases to remove dissolved dioxygen. Then the electrode was illuminated by a solar simulator. The effect of the photodeposition parameters was investigated by using different illumination times (90, 60, and 30 s), illumination intensities (100, 44, 30 mW cm^{-2}), and H_2PtCl_6 concentrations (1, 5, and 10 mM).

2.5. Characterization

The morphology of SnSe flakes was analyzed using scanning electron microscopy (SEM, Hitachi S-4700 Type II) equipped with energy dispersive X-ray spectroscopy (EDS) probe. Transmission electron microscopy (TEM) images were recorded on a FEI Tecnai G2 20 X-Twin type instrument, operating at 200 kV. The area and perimeter of SnSe flakes were analyzed with ImageJ software. The thickness of SnSe flakes was measured using NT-MDT Solver atomic force microscope (AFM) operated in the "tapping" mode with a silicon tip on a silicon nitride lever. Laser Raman spectra were recorded on a Senterra II Compact Raman microscope (Bruker) using a green laser ($\lambda = 532$ nm), operating at a power of ≤ 2.5 mW. X-ray photoelectron spectroscopy (XPS) (Mg Kα) was carried out on a SPECS instrument equipped with a PHOIBOS 150 MCD 9 hemispherical analyzer. The analyzer was used in the transmission mode with 40 eV pass energy for the survey scans and 20 eV pass energy for the high-resolution scans. Charge referencing was done to adventitious carbon (284.8 eV) on the sample surface as reference. For XPS band deconvolution, CasaXPS commercial software package was used.

2.6. Photoelectrochemical measurements

PEC HER performance of the SnSe photoelectrodes was tested with an electrochemical workstation (Bio-logic SAS VMP-300) in a three-electrode configuration. SnSe-coated GC was the working electrode, while GC plate as counter electrode, and Ag/AgCl reference electrode (3 M NaCl, BASi®) were applied. The potential values were converted to the reversible hydrogen electrode (RHE) scale using the equation of $E_{RHE} = E_{Ag/AgCl} + 0.210\ V + 0.0591 \times pH$. Linear sweep photovoltammetry was recorded in argon (Ar, Messer, 99.996%) saturated 0.5 M H_2SO_4 with the scan rate of 2.5 mV s^{-1}, under chopped illumination (on/off, 10 s/10 s) (Newport LCS-100 solar simulator, 100 mW cm^{-2} flux). Long term chronoamperometry was performed for 1 h in Ar-saturated 0.5 M H_2SO_4, under chopped illumination (on/off, 30 s/30 s) at a constant potential of − 0.54 V vs. RHE.

Incident photon-to-electron conversion efficiency (IPCE) measurements were carried out on a Newport Quantum Efficiency Measurement System (QEPVSI-B). IPCE values were calculated using the following equation: IPCE (%) = (1240 × j) × 100/(P × λ), where j, P, and λ refer to the photocurrent density at − 0.54 V vs. RHE, photon flux, and wavelength, respectively. Intensity modulated photocurrent spectroscopy (IMPS) was performed on the SnSe electrodes using the same configuration as described in the cases of photovoltammetry and IPCE measurements, using an AUTOLAB PGSTAT302N potentiostat equipped with a FRA32 module and a light-emitting diode (LED) driver kit (Metrohm-Autolab). The spectra were recorded in the frequency range between 20 kHz and 0.1 Hz, applying a sinusoidal light intensity modulation and bias illumination using a white light LED, in 0.5 M H_2SO_4 solution. The amplitude of the sinusoidal modulation was ~10% of the original intensity.

3. Results and discussion

The morphology of the SnSe flakes obtained by exfoliation was investigated by SEM and AFM. Fig. 3a and b show the SEM and AFM images of IPA-SnSe, which exhibits angular shapes. To quantify the size of the flakes, the area and perimeter were determined by the SEM images, while the thickness was measured by AFM. The average area and thickness of IPA/H_2O-SnSe and IPA-SnSe were found to be 4.0 ± 1.3 μm^2, 2.8 ± 0.9 μm^2, and 297 ± 189 nm, 266 ± 119 nm respectively. The statistical analysis of the morphology characteristics is shown in Fig. S1. A log-normal fit was employed, as such distribution is characteristic of a random multiplicative process, for example ball milling, cavitation, representing that the exfoliation follows a linear fragmentation model (process is driven by an external source, such as ultrasonic

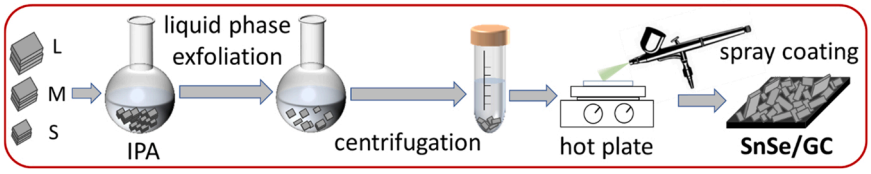

Fig. 2. Schematic illustration of liquid phase exfoliation of the size-selected SnSe crystals, selection of flakes using centrifugation, and preparation of SnSe flake-based electrodes.

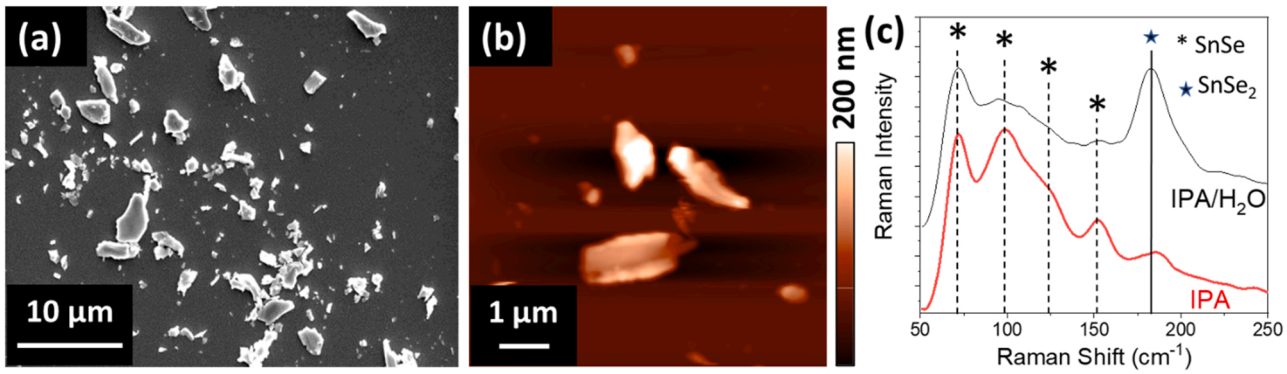

Fig. 3. Morphological and structural characterization of the SnSe flakes. (a) SEM and (b) AFM images of selected IPA exfoliated flakes. (c) Representative laser Raman spectra of SnSe samples exfoliated in different solvents. The dashed and solid lines correspond to the SnSe and $SnSe_2$ vibration bands, respectively.

waves) [46,47]. The mode values of the morphology characteristics are listed in Table S1. Exfoliation in IPA/H_2O resulted larger average area, perimeter, and thickness compared to flakes prepared in IPA. The edge density was calculated by dividing the perimeter by the area: the IPA-SnSe samples had higher edge density compared to IPA/H_2O-SnSe, in good agreement with the literature [7,48].

Laser Raman spectroscopy was employed to investigate the atomic vibrational modes in the SnSe flakes (Fig. 3c). Regardless of the solvent used for the exfoliation, four characteristic peaks were found in the samples at 72.0, 99.1, 124.5, and 152 cm^{-1} corresponding to A_g^1, B_g^3, A_g^2, and A_g^3 vibrational modes of SnSe, respectively [49]. An additional peak located at ~ 182.5 cm^{-1} was identified as the Raman active A_g^1 mode of $SnSe_2$, corresponding to in-plane vibrations [50]. This latter mode is more prominent in the case of IPA/H_2O-SnSe, compared to IPA-SnSe. The presence of $SnSe_2$ in SnSe samples has been reported earlier [19,51]. $SnSe_2$ is an n-type semiconductor with an energy bandgap ~ 1.5–2.2 eV, varied in the function of thickness [29,52–54], which can be formed by nonstoichiometric combination of Sn and Se or local phase segregation during SnSe formation [17,55].

Linear sweep photovoltammograms (LSV) of SnSe films showed p-type photoactivity for both IPA/H_2O-SnSe (SnSe loading: 0.29 ± 0.03 mg cm^{-2}) and IPA-SnSe electrodes (SnSe loading: 0.28 ± 0.06 mg cm^{-2}) (Fig. 4a). The photocurrent gradually increased at more negative potentials. The IPA-SnSe electrode gave higher photocurrent density (calculated by subtracting dark current density from total current density from the LSV curves) compared to the IPA/H_2O-SnSe electrode, yet it was coupled with a higher dark current, which can be explained by the higher edge density of IPA-SnSe flakes [56]. The small fraction of $SnSe_2$ phase in the SnSe sample might improve the PEC properties, as reported previously [17,57]. The $SnSe_2$ as the secondary phase, however, destroys the stacking order of SnSe, and produces more defects inside of SnSe sheets [58], which becomes a recombination center for the charge carriers. Based on the Raman spectra (Fig. 3c), more $SnSe_2$ was found in the IPA/H_2O-SnSe case.

The effect of the solvent used in the LPE process on the PEC performance was further investigated using 4 different IPA/H_2O mixtures. The photocurrent density values decreased by reducing the IPA content in the exfoliation solvent mixture of IPA/H_2O (Fig. 4b). The IPA/H_2O (1:0) electrodes showed 1.18 mA cm^{-2} photocurrent density at −0.69 V vs. RHE, which was 10 times higher compared with IPA/H_2O (1:3) (0.11 mA cm^{-2}) case. The averaged values presented on Fig. 4b at four different potentials were obtained for 3 different electrodes for each SnSe sample. The mixture of IPA/H_2O with varying ratios had different surface tensions, which in turn facilitated different interactions between the solvent and the SnSe crystals during the exfoliation process. This can result in different morphologies and product yields [59]. The overall yield of exfoliation for SnSe flakes was calculated by using the equation: *overall yield = mass of flakes / starting SnSe mass* [60]. IPA-SnSe showed

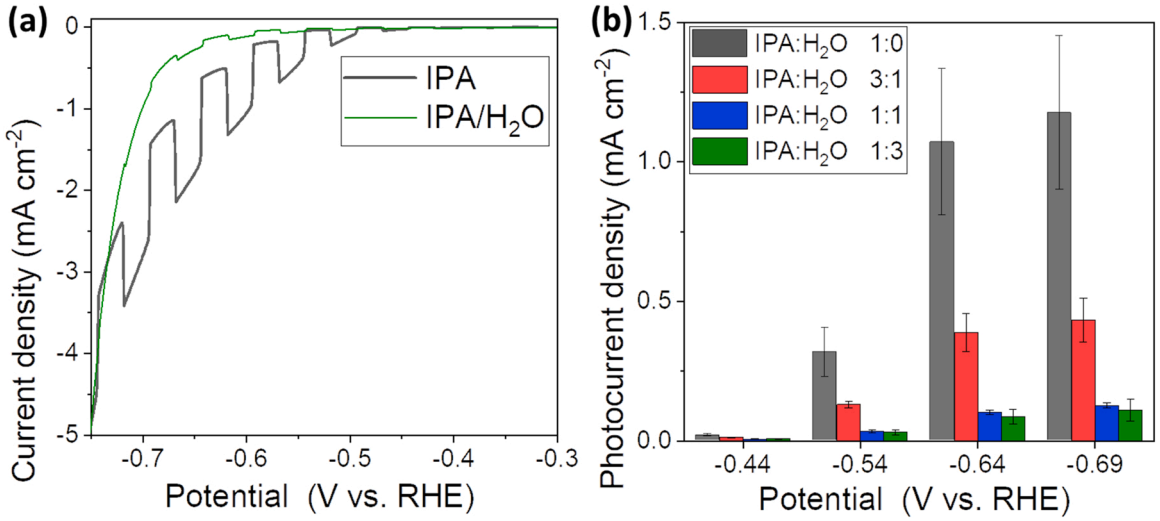

Fig. 4. (a) Linear sweep photovoltammograms of electrodes derived from SnSe flakes [the flakes were obtained by exfoliating ar-SnSe in different IPA/H_2O mixtures (IPA: H_2O = 1:0 and 1:3)] at 2.5 mV s^{-1} sweep rate, in Ar saturated 0.5 M H_2SO_4 solution. (b) Bar diagrams of photocurrent density of electrodes made from SnSe flakes obtained by exfoliating ar-SnSe in different IPA/H_2O mixtures (IPA: H_2O = 1:0, 3:1, 1:1, 1:3) at four different potentials. The averaged values and error bars were obtained of 3 replicate electrodes for each case.

higher yield (63%) than IPA/H_2O-SnSe (25%).

The effect of flake size on the PEC HER performance was also investigated applying a sieve-based method to prepare SnSe suspensions with controllable particle size. Size-selected SnSe crystals were then exfoliated in IPA, according to the process shown in Fig. 2 above (noted as L-IPA-, M-IPA-, S-IPA-SnSe). Table 2 shows the yield values of L-, M-, S-SnSe upon exfoliation in IPA, showing an increasing overall yield with decreasing initial SnSe crystal size. TEM and AFM measurements confirmed that all specimens exhibited random angular shape (Fig. S2) and smaller size (Fig. S3, Table S2) than those obtained by exfoliating the ar-SnSe crystals. The S-IPA-SnSe showed a more monodispersed distribution than the other 2 fractions, which may be traced to the original narrower SnSe crystal size distribution.

Spray coating was employed instead of m-LB method to have a better control on the catalyst loading of the electrodes. The loading dependence of the PEC performance in the case of L-IPA-SnSe is presented in Fig. S4. The optimal loading of the SnSe film on GC was identified as 0.3 mg cm^{-2}. The effect of flake dimensions on the PEC HER performance was compared applying the optimal 0.3 mg cm^{-2} loading for other sized catalysts as well (Fig. 5a). No significant PEC activity difference was observed among the differently sized sample (Fig. 5b). L-, M- and S-IPA-SnSe showed the maximum photocurrent densities of 2.44 $\pm$ 0.65, 2.34 $\pm$ 0.19 and 2.14 $\pm$ 0.34 mA cm^{-2} at −0.74 V vs. RHE, respectively. These all displayed higher PEC activity than IPA-SnSe (1.18 $\pm$ 0.28 mA cm^{-2}) demonstrating that the spray-coating and sieve-based method conspired to achieve higher PEC activity.

To test the stability of the SnSe electrodes, 1 h long chronoamperometry measurement was performed under continuous stirring and chopped illumination (on/off every 30 s) at −0.54 V vs. RHE of the L-IPA-SnSe photocathode (Fig. 5c). The sample still exhibited 52% of the initial activity after 1 h, indicating a relatively good stability. The PEC activity of the exfoliated SnSe flakes was studied as a function of the storage time of their suspension to check their stability in IPA. For this purpose, the fresh L-IPA-SnSe suspension was divided into several portions. These were purged with Ar gas, sealed into the vial, and kept under dark, cooled condition. Each week, one of the portions was spray coated on GC with SnSe loading of 0.3 mg cm^{-2} and measured. The fresh one was considered as a reference. The photocurrent density gradually decreased (Fig. S5). The SnSe flakes in the IPA did not appear to be stable under the conditions employed, restacking could have occurred [20]; this possibility needs further investigation. Therefore, the results presented in this work were recorded on fresh samples.

The internal-photon-to-electron-conversion-efficiency (IPCE) of L-IPA-SnSe is shown on Fig. 5d. The sample presented the highest conversion efficiency at 900 nm which is due to the narrow bandgap of SnSe (1.1 eV) [61]. Additionally, two maximal values were found (550 nm) and 900 nm), representing the different absorption characteristics of $SnSe_2$ and SnSe, respectively. The IPCE spectra of L-, M- and S-IPA-SnSe electrodes in Fig. S6 displayed same absorption edge and similar absorption, indicating similar compositions. The corresponding $SnSe_2$ phase in the electrode material was detected by IPCE measurement and Raman spectroscopy (Fig. 3c). The presence of this phase can improve the charge carrier separation and the interfacial charge transfer compared to pure SnSe, as reported previously [17,57].

To enhance the PEC HER performance of SnSe, Pt islands were deposited on SnSe electrode by the photodeposition method. In this case, the S-IPA-SnSe was employed as bare SnSe reference. Figs. S7a, b and c show the photocurrent densities of Pt decorated SnSe with different photodeposition parameters (irradiation time, irradiation power density, Pt precursor concentration) recorded at 5 potentials. The optimum Pt deposition parameters were 60 s illumination time, 44 mW cm^{-2} illumination intensity and 5 mM H_2PtCl_6. XPS was employed to investigate the surface elemental composition of bare and Pt decorated SnSe. As shown in Fig. S8, two peaks appeared at binding eneries of 76.1 and 72.6 eV were ascribed to Pt 4 $f_{5/2}$ and 4 $f_{7/2}$, respectively, indicating the deposition of Pt on SnSe surface. Fig. 6a shows representative photovoltammograms of bare and Pt decorated SnSe prepared under these optimal deposition conditions. Clearly, for Pt decorated SnSe: i) notably higher photocurrents were achieved; ii) dark currents were higher and started to develop earlier; iii) the onset potential shifted to more positive potential. The onset potential (ca. −0.25 V) of PEC HER on Pt decorated SnSe electrodes is more negative than the desired positive than 0 V vs. RHE. This issue could be explained by the effect of structural domains (i.e., in plane defects, edges, and thickness of sheets) on the PEC activity of TMDCs [14,48,62]. The PEC HER activity of thermal vacuum prepared SnSe thin films has been investigated recently, in the function of selenization time, to repair defects aiming to improve the PEC activity. Such treatment increased the photocurrent and shifted the onset potential to a more positive value [20]. Fig. 6b shows that SnSe electrodes with Pt catalyst could yield two-times higher photocurrent than bare SnSe (i.e., 4.39 mA cm^{-2}).

IMPS was employed to investigate the effect of Pt catalyst on the charge carrier transfer and recombination kinetics [40,63]. Fig. 7a and b show a set of IMPS spectra for bare and Pt decorated SnSe recorded at different potentials ranging from –0.24 to −0.67 V vs. RHE. Two semicircles could be found in the 3rd and 2nd quadrant, typical of the behaviour for p-type semiconductors [64]. Almost perfect circles could be found at less negative potentials, meaning that the measured steady-state photocurrent was close to zero. Thus, surface recombination dominated the PEC behaviour of the system. No upper semicircle was observed below −0.67 V vs. RHE for bare SnSe, and below −0.57 V for Pt decorated SnSe. Kinetic parameters, charge carrier transfer (k_{tr}) and surface recombination (k_{sr}) could be determined from the IMPS data, and are plotted versus applied potential in Fig. 7c and d. After Pt deposition, the electrode showed higher k_{tr} values at same potential until −0.5 V vs. RHE. Smaller k_{sr} was determined for Pt decorated SnSe below −0.3 V vs. RHE, as expected from Pt supressing the charge carrier recombination. The Cole–Cole plot is showed in Fig. S9 for bare and Pt-decorated SnSe electrodes as the function of the applied potential determined from the IMPS data. There is a peak on the spectra around 2.5 kHz and 2.2 kHz for bare SnSe, and Pt decorated SnSe electrodes, respectively. This peak can be attributed to the charge transport [65] in the SnSe film, representing higher imaginary frequency dependent EQE for Pt decorated SnSe.

The relative transfer efficiency can be calculated by the equation: $\eta_{tr} = k_{tr}/(k_{tr+} k_{sr})$ [66]. As shown in Fig. 6c, significantly enhanced η_{tr} values were found in the case of Pt decorated SnSe electrodes. At more negative potentials, however, bare SnSe can also reach a similar η_{tr} (~90%). The processes taking place at the bare and cocatalyst decorated SnSe are summarized in Fig. 8. In the case of bare SnSe, electrons, excited to the conduction band, can either move to the surface states and recombine with valence band holes (1) or directly reduce H^+ to H_2 (2). The first means that electrons do not participate in HER. Depositing Pt nanoparticles on the surface can passivate the surface states, thereby inhibiting charge carrier recombination (1). Meanwhile, the electrons can be transferred to Pt, then reduce H^+ directly via Pt (3) [67]. This dual role of Pt results in the enhancement of the PEC HER activity for SnSe.

Table 2
The overall yield of SnSe fractions exfoliated in IPA.

Fractions	Overall yield (%)
L-IPA-SnSe	5.6 $\pm$ 0.2
M-IPA-SnSe	17.1 $\pm$ 0.8
S-IPA-SnSe	85.3 $\pm$ 8.5

4. Conclusions

In this work, we fabricated macroscopic photocathodes by depositing SnSe flakes, made from commercial SnSe crystals using a LPEx method, on glassy carbon. The as-received SnSe crystals were exfoliated in IPA or

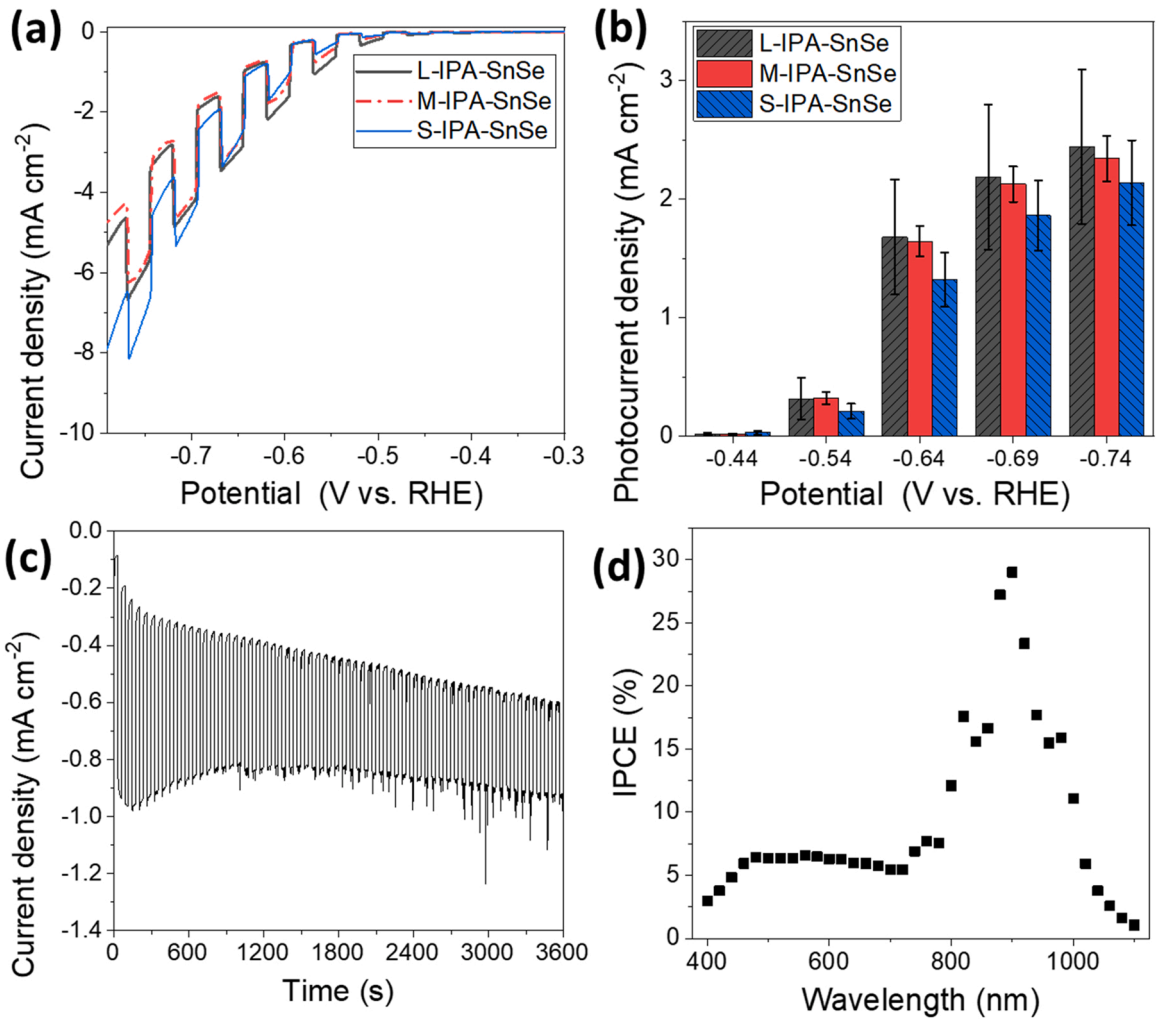

Fig. 5. (a) Linear sweep photovoltammograms of electrodes made from SnSe flakes (obtained by exfoliating size separated (L, M, S) SnSe in IPA) with 2.5 mV s^{-1} sweep rate, in Ar saturated 0.5 M H_2SO_4 solution. (b) Bar diagrams of photocurrent density of the electrodes made from SnSe flakes obtained by exfoliating size separated (L, M, S) SnSe in IPA at five different potentials. The averaged value and error bars were obtained over 3 replicate electrodes for each case. (c) Transient photocurrent density profile and (d) quantum efficiency curve of L-IPA-SnSe electrode. The data in panels (c) and (d) were acquired at a fixed potential of −0.54 V vs. RHE.

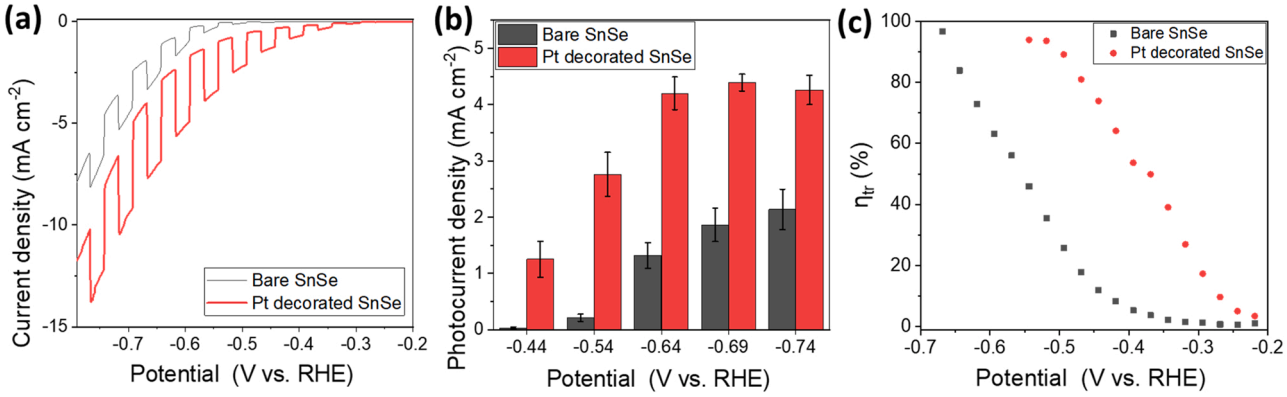

Fig. 6. (a) Photovoltammograms for the illuminated cells assembled with bare and Pt decorated SnSe electrodes. (b) Bar diagram of photocurrents plotted versus the potential, and (c) the determined charge transfer efficiency as a function of applied potential for bare and Pt decorated SnSe electrodes.

IPA/H_2O mixture. Pure IPA was found to be the optimal solvent to prepare flakes and for achieving the highest PEC activity. A sieve-based method was further employed to separate the as-received SnSe crystals to three different size fractions. These size-selected crystals were also exfoliated in IPA, and the PEC activity of the photocathodes made from them were investigated. These samples showed a maximum photocurrent of 2.44 mA cm^{-2}, twice higher than using as-received crystal exfoliated in pure IPA.

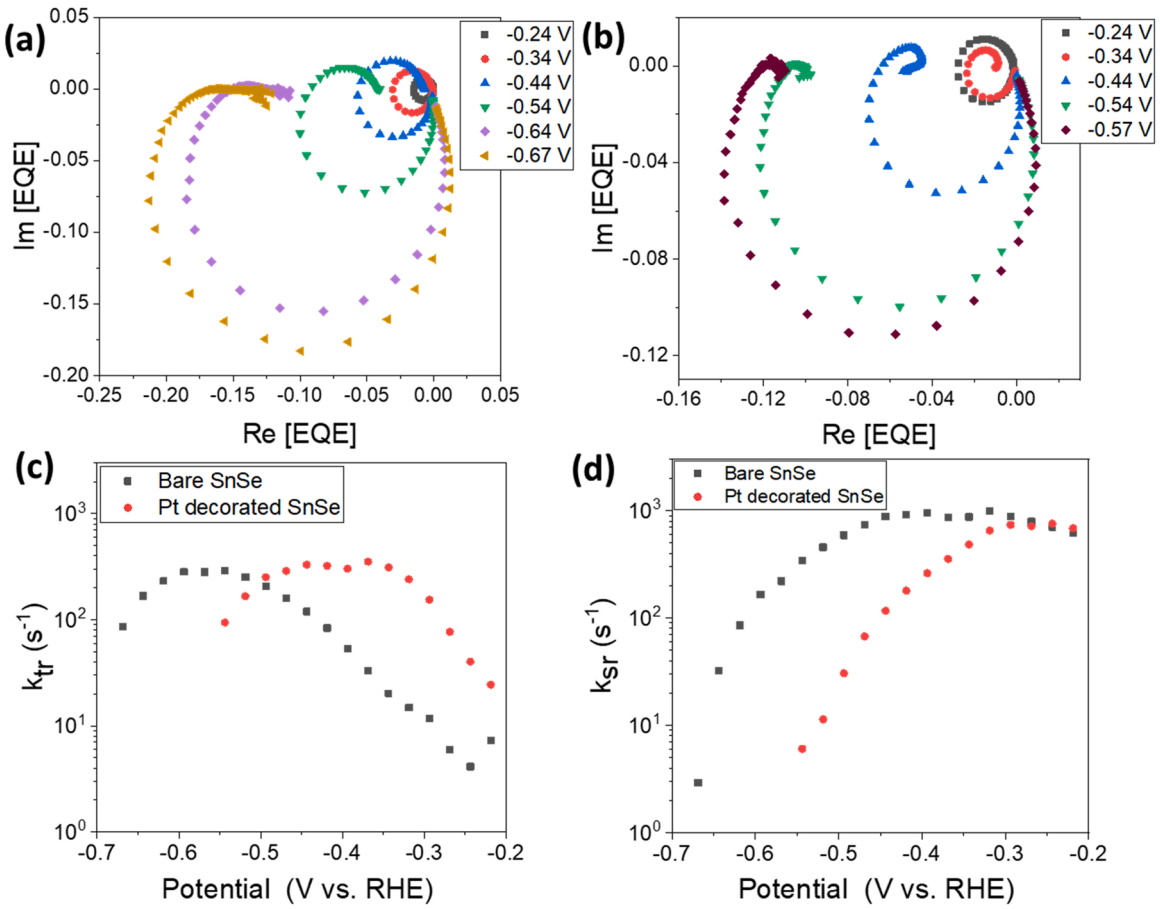

Fig. 7. IMPS data for (a) bare and (b) Pt decorated SnSe electrodes. Measured 25 mV potential step (only some potentials showed here). (c) Charge transfer and (d) recombination rate constants as the function of the applied potential determined from the IMPS data.

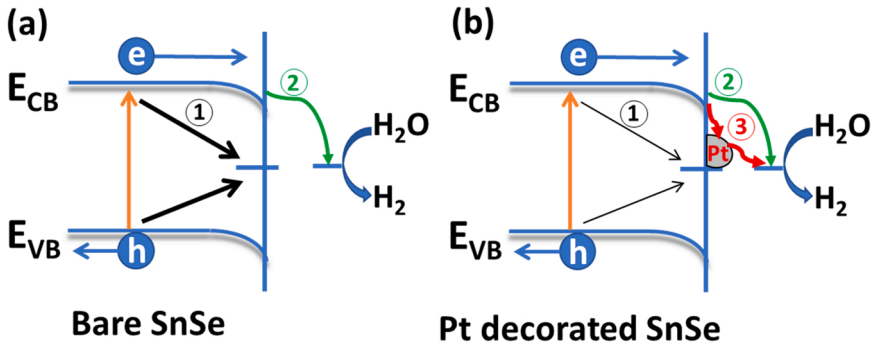

Fig. 8. Simplified model of the elementary processes in (a) bare SnSe, and (b) Pt decorated SnSe electrodes. Upon illumination, photogenerated carriers move towards the semiconductor-electrolyte interface, (1) surface state-mediated recombination of electron-hole pairs, (2) electron transfer directly from the conduction band to the electrolyte, (3) electron transfer to the electrolyte via Pt.

Platinum catalyst islands were photodeposited on the surface of SnSe, and different deposition parameters were investigated. The best performance was 4.39 mA cm^{-2}, twice higher than bare SnSe. IMPS results showed that the Pt catalyst improved charge transfer kinetics and also supressed charge carrier recombination. Overall, the solvent for exfoliation, the edge density of SnSe flakes, immobilization method and Pt co-catalyst affected the PEC HER performance. By optimizing these factors, the photocurrent density of SnSe was enhanced from 0.11 to 4.39 mA cm^{-2}. These results indicate the merit of employing SnSe electrodes for PEC HER and afford further opportunities for exploring PEC processes on such 2D electrodes.

CRediT authorship contribution statement

Qianqian Ba: Investigation, Data curation, Writing – original draft. **Péter S. Tóth:** Methodology, Investigation, Data curation, Writing – original draft, Supervision. **Ádám Vass:** Investigation. **Krishnan Rajeshwar:** Conceptualization, Writing – review & editing. **Csaba Janáky:** Conceptualization, Methodology, Resources, Writing – review & editing, Supervision.

Declaration of Competing Interest

The authors declare that they have no known competing financial

interests or personal relationships that could have appeared to influence the work reported in this paper.

Data Availability

Data will be made available on request.

Acknowledgment

Project no. RRF-2.3.1-21-2022-00009, titled National Laboratory for Renewable Energy has been implemented with the support provided by the Recovery and Resilience Facility of the European Union within the framework of Programme Széchenyi Plan Plus. This paper was supported by the János Bolyai Research Scholarship of the Hungarian Academy of Sciences and the ÚNKP-22-5 – New National Excellence Program of the Ministry for Innovation and Technology from the Source of National Research, Development and Innovation Fund. Q.Q.B. would like to thank the Stipendium Hungaricum scholarship and the China Scholarship Council for a PhD scholarship.

Conflict of interest

There are no conflicts to declare.

Supporting information

Supporting Information is available online, including morphological characterization, further photoelectrochemical activity of SnSe specimens, IPCE and XPS data.

Appendix A. Supporting information

Supplementary data associated with this article can be found in the online version at doi:10.1016/j.apcata.2023.119233.

References

[1] S.E. Hosseini, M.A. Wahid, Renew. Sustain. Energy Rev. 57 (2016) 850–866.
[2] K. Rajeshwar, R. McConnell, S. Licht, Solar Hydrogen Generation: Toward a Renewable Energy Future, 2008.
[3] M.A. Marwat, M. Humayun, M.W. Afridi, H. Zhang, M.R. Abdul Karim, M. Ashtar, M. Usman, S. Waqar, H. Ullah, C. Wang, W. Luo, ACS Appl. Energy Mater. 4 (2021) 12007–12031.
[4] E. Kecsenovity, B. Endrődi, P.S. Tóth, Y. Zou, R.A.W. Dryfe, K. Rajeshwar, C. Janáky, J. Am. Chem. Soc. 139 (2017) 6682–6692.
[5] W. Li, H. Wang, Z. Sun, Q. Wu, S. Xue, J. Power, Sources 492 (2021), 229667.
[6] K.K. Paul, N. Sreekanth, R.K. Biroju, A.J. Pattison, D. Escalera-López, A. Guha, T. N. Narayanan, N.V. Rees, W. Theis, P.K. Giri, J. Mater. Chem. A 6 (2018) 22681–22696.
[7] X. Yu, K. Sivula, Chem. Mater. 29 (2017) 6863–6875.
[8] S. Seo, S. Kim, H. Choi, J. Lee, H. Yoon, G. Piao, J.C. Park, Y. Jung, J. Song, S. Y. Jeong, H. Park, S. Lee, Adv. Sci. 6 (2019).
[9] J. Zheng, Y. Lyu, R. Wang, C. Xie, H. Zhou, S.P. Jiang, S. Wang, Nat. Commun. 9 (2018) 1–10.
[10] R.J. Britto, J.L. Young, Y. Yang, M.A. Steiner, D.T. Lafehr, D.J. Friedman, M. Beard, T.G. Deutsch, T.F. Jaramillo, J. Mater. Chem. A 7 (2019) 16821–16832.
[11] A.M. Beiler, D. Khusnutdinova, S.I. Jacob, G.F. Moore, ACS Appl. Mater. Interfaces 8 (2016) 10038–10047.
[12] I.S. Kwon, I.H. Kwak, T.T. Debela, H.G. Abbas, Y.C. Park, J.P. Ahn, J. Park, H. S. Kang, ACS Nano 14 (2020) 6295–6304.
[13] H. Coskun, F.H. Isikgor, Z. Chen, M. Imran, B. Li, Q. Xu, J. Ouyang, J. Mater. Chem. A 7 (2019) 4759–4765.
[14] P.S. Tóth, G. Szabó, C. Janáky, J. Phys. Chem. C 125 (2021) 7701–7710.
[15] Y. Son, Q.H. Wang, J.A. Paulson, C.-J. Shih, A.G. Rajan, K. Tvrdy, S. Kim, B. Alfeeli, R.D. Braatz, M.S. Strano, ACS Nano 9 (2015) 2843–2855.
[16] P.S. Tóth, G. Szabó, C. Janáky, J. Phys. Chem. C 125 (2021) 7701–7710.
[17] Z. Wang, C. Fan, Z. Shen, C. Hua, Q. Hu, F. Sheng, Y. Lu, H. Fang, Z. Qiu, J. Lu, Z. Liu, W. Liu, Y. Huang, Z.A. Xu, D.W. Shen, Y. Zheng, Nat. Commun. 9 (2018).
[18] H. Ju, J. Kim, ACS Nano 10 (2016) 5730–5739.
[19] L. Hao, Y. Du, Z. Wang, Y. Wu, H. Xu, S. Dong, H. Liu, Y. Liu, Q. Xue, Z. Han, K. Yan, M. Dong, Nanoscale 12 (2020) 7358–7365.
[20] R. Wang, Y. Lyu, S. Du, S. Zhao, H. Li, L. Tao, S.P. Jiang, J. Zheng, S. Wang, J. Mater. Chem. A 8 (2020) 5342–5349.
[21] Y.K. Lee, Z. Luo, S.P. Cho, M.G. Kanatzidis, I. Chung, Joule 3 (2019) 719–731.
[22] S.H. Heo, S. Jo, H.S. Kim, G. Choi, J.Y. Song, J.Y. Kang, N.J. Park, H.W. Ban, F. Kim, H. Jeong, J. Jung, J. Jang, W.B. Lee, H. Shin, J.S. Son, Nat. Commun. 10 (2019).
[23] S. Gowthamaraju, U.P. Deshpande, P.A. Bhobe, J. Mater. Sci. Mater. Electron. 32 (2021) 11781–11790.
[24] K. Patel, P. Chauhan, A.B. Patel, G.K. Solanki, K.D. Patel, V.M. Pathak, ACS Appl. Nano Mater. 3 (2020) 11143–11151.
[25] X. Liu, Y. Li, B. Zhou, X. Wang, A.N. Cartwright, M.T. Swihart, Chem. Mater. 26 (2014) 3515–3521.
[26] D. Zheng, H. Fang, M. Long, F. Wu, P. Wang, F. Gong, X. Wu, J.C. Ho, L. Liao, W. Hu, ACS Nano 12 (2018) 7239–7245.
[27] Y. Huang, L. Li, Y.H. Lin, C.W. Nan, J. Phys. Chem. C 121 (2017) 17530–17537.
[28] Z. Jia, J. Xiang, F. Wen, R. Yang, C. Hao, Z. Liu, ACS Appl. Mater. Interfaces 8 (2016) 4781–4788.
[29] H. Zhao, Y. Yan, C. Xia, X. Song, A. Dong, J. Su, J. Li, J. Phys. D Appl. Phys. 53 (2020).
[30] B. Subramanian, T. Mahalingam, C. Sanjeeviraja, M. Jayachandran, M. J. Chockalingam, Thin Solid Films 357 (1999) 119–124.
[31] C. Lu, Y. Zhang, L. Zhang, Q. Yin, Appl. Surf. Sci. 484 (2019) 560–567.
[32] A. Lukinskas, V. Jasulaitiene, P. Lukinskas, I. Savickaja, P. Kalinauskas, Electrochim. Acta 51 (2006) 6171–6178.
[33] F. Li, H. Chen, L. Xu, F. Zhang, P. Yin, T. Yang, T. Shen, J. Qi, Y. Zhang, D. Li, Y. Ge, H. Zhang, ACS Appl. Mater. Interfaces 13 (2021) 33226–33236.
[34] J. Fan, X. Huang, F. Liu, L. Deng, G. Chen, Compos. Commun. 24 (2021), 100612.
[35] Y. Ye, Y. Xian, J. Cai, K. Lu, Z. Liu, T. Shi, J. Du, Y. Leng, R. Wei, W. Wang, X. Liu, G. Bi, J. Qiu, Adv. Opt. Mater. 7 (2019) 1800579.
[36] X. Yu, M.S. Prévot, N. Guijarro, K. Sivula, Nat. Commun. 6 (2015).
[37] J. Kim, S. Kwon, D.H. Cho, B. Kang, H. Kwon, Y. Kim, S.O. Park, G.Y. Jung, E. Shin, W.G. Kim, H. Lee, G.H. Ryu, M. Choi, T.H. Kim, J. Oh, S. Park, S.K. Kwak, S. W. Yoon, D. Byun, Z. Lee, C. Lee, Nat. Commun. 6 (2015).
[38] C. Backes, B.M. Szydłowska, A. Harvey, S. Yuan, V. Vega-Mayoral, B.R. Davies, P. Zhao, D. Hanlon, E.J.G. Santos, M.I. Katsnelson, W.J. Blau, C. Gadermaier, J. N. Coleman, ACS Nano 10 (2016) 1589–1601.
[39] A. Vega-Poot, M. Rodríguez-Pérez, J. Becerril-González, I. Rodríguez-Gutiérrez, J. Su, G. Rodríguez-Gattorno, W.Y. Teoh, G. Oskam, J. Electrochem. Soc. 169 (2022), 056519.
[40] J.E. Thorne, Y. Zhao, D. He, S. Fan, S. Vanka, Z. Mi, D. Wang, Phys. Chem. Chem. Phys. 19 (2017) 29653–29659.
[41] C. Tossi, L. Hällström, J. Selin, M. Vaelma, E. See, J. Lahtinen, I. Tittonen, J. Mater. Chem. A 7 (2019) 14519–14525.
[42] M. Yamamoto, Y. Minoura, M. Akatsuka, S. Ogawa, S. Yagi, A. Yamamoto, H. Yoshida, T. Yoshida, Phys. Chem. Chem. Phys. 22 (2020) 8730–8738.
[43] X. Yu, M.S. Prévot, N. Guijarro, K. Sivula, Nat. Commun. 6 (2015) 7596.
[44] F. Bozheyev, K. Harbauer, C. Zahn, D. Friedrich, K. Ellmer, Sci. Rep. 7 (2017) 16003.
[45] X. Jiang, B. Sun, Y. Song, M. Dou, J. Ji, F. Wang, RSC Adv. 7 (2017) 49309–49319.
[46] Z. Cheng, S. Redner, Phys. Rev. Lett. 60 (1988) 2450–2453.
[47] K. Kouroupis-Agalou, A. Liscio, E. Treossi, L. Ortolani, V. Morandi, N.M. Pugno, V. Palermo, Nanoscale 6 (2014) 5926–5933.
[48] M.A. Todt, A.E. Isenberg, S.U. Nanayakkara, E.M. Miller, J.B. Sambur, J. Phys. Chem. C 122 (2018) 6539–6545.
[49] S. Zhao, H. Wang, Y. Zhou, L. Liao, Y. Jiang, X. Yang, G. Chen, M. Lin, Y. Wang, H. Peng, Z. Liu, Nano Res. 8 (2015) 288–295.
[50] C. Gurnani, S.L. Hawken, A.L. Hector, R. Huang, M. Jura, W. Levason, J. Perkins, G. Reid, G.B.G. Stenning, Dalton Trans. 47 (2018) 2628–2637.
[51] Z. Tian, M. Zhao, X. Xue, W. Xia, C. Guo, Y. Guo, Y. Feng, J. Xue, ACS Appl. Mater. Interfaces 10 (2018) 12831–12838.
[52] M. Kumar, S. Rani, Y. Singh, K.S. Gour, V.N. Singh, RSC Adv. 11 (2021) 6477–6503.
[53] D. Martínez-Escobar, M. Ramachandran, A. Sánchez-Juárez, J.S. Narro Rios, Thin Solid Films 535 (2013) 390–393.
[54] S. Saha, A. Banik, K. Biswas, Chem. A Eur. J. 22 (2016) 15634–15638.
[55] W. Albers, J. Verbekt, J. Mater. Sci. 5 (1970) 24–28.
[56] J. Kibsgaard, Z. Chen, B.N. Reinecke, T.F. Jaramillo, Nat. Mater. 11 (2012) 963–969.
[57] B. Qin, Y. Zhang, D. Wang, Q. Zhao, B. Gu, H. Wu, H. Zhang, B. Ye, S.J. Pennycook, L.D. Zhao, J. Am. Chem. Soc. 142 (2020) 5901–5909.
[58] M. Kumar, P. Sharma, S. Rani, M. Kumar, V.N. Singh, AIP Adv. 11 (2021), 025040.
[59] U. Halim, C.R. Zheng, Y. Chen, Z. Lin, S. Jiang, R. Cheng, Y. Huang, X. Duan, Nat. Commun. 4 (2013) 1–7.
[60] Y. Hernandez, V. Nicolosi, M. Lotya, F.M. Blighe, Z. Sun, S. De, I.T. McGovern, B. Holland, M. Byrne, Y.K. Gun'ko, J.J. Boland, P. Niraj, G. Duesberg, S. Krishnamurthy, R. Goodhue, J. Hutchison, V. Scardaci, A.C. Ferrari, J. N. Coleman, Nat. Nanotechnol. 3 (2008) 563–568.
[61] A.K. Deb, V. Kumar, Phys. Status Solidi Basic Res 254 (2017) 1600379.
[62] J.W. Hill, C.M. Hill, Nano Lett. 19 (2019) 5710–5716.
[63] L. Peter, J. Electrochem. Soc. 166 (2019) H3125–H3132.
[64] E.A. Ponomarev, L.M. Peter, J. Electroanal. Chem. 397 (1995) 45–52.
[65] G.R. Neupane, M. Bamidele, V. Yeddu, D.Y. Kim, P. Hari, J. Mater. Res. 37 (2022) 1357–1372.
[66] M. Rodríguez-Pérez, I. Rodríguez-Gutiérrez, A. Vega-Poot, R. García-Rodríguez, G. Rodríguez-Gattorno, G. Oskam, Electrochim. Acta 258 (2017) 900–908.
[67] C. Zachäus, F.F. Abdi, L.M. Peter, R. Van De Krol, Chem. Sci. 8 (2017) 3712–3719.